Climate Dynamics (2025) 63:42
https://doi.org/10.1007/s00382-024-07539-x

Heat waves in India: patterns, associations, and subseasonal prediction skill

Raju Mandal[1] · Susmitha Joseph[1] · Shubham Waje[1] · Anurag Chaudhary[1] · Avijit Dey[1] · Mahesh Kalshetti[1] · A. K. Sahai[1]

Received: 8 February 2024 / Accepted: 3 December 2024 / Published online: 17 December 2024

Abstract
Heat waves (HWs) in India during March–June and from 1951 to 2023 are thoroughly analysed in this work, emphasising trends, decadal variations, and related large-scale features. Average HW days per decade and anomalies are computed using HW criteria based on high-resolution maximum temperature (Tmax) data. The findings indicate a notable increase in HW occurrence in the central, southeast, and northwest regions after the year 2000. Month-wise analyses reveal detailed patterns, showcasing increased HW days in non-traditionally hot months, like March in southern regions. This suggests an intensification of extreme summer conditions over both time and across different regions. Examining the spatial HW trends exposes a notable increase in total HW days/year over northwest, central and south-eastern regions, while few others witness decreasing trends. The study reveals significant increasing trends in the total number of HW days in the two HW-prone regions, Northwest (NW) and Southeast (SE), from 1951 to 2023, where HW spells have also become more persistent. Three types of HW spells are analysed: NW-spells and SE-spells, defined by area-averaged daily Tmax exceeding 43 °C and 40 °C, respectively, for six consecutive days, and NWSE-spells, where HW periods overlap between the two regions. The analysis of large-scale characteristics associated with these HW spells emphasises the possible role of oceans and atmospheric variables in HW patterns. These findings highlight the importance of improving predictive capabilities for HWs. To this end, the extended range prediction system version 2 (ERPSv2) is introduced in this study, assessing its subseasonal prediction skill. The results demonstrate that ERPSv2 performs better than its predecessor, ERPSv1, particularly with a three-week lead time. Validation through a case study on the June 2023 HW disaster showcases ERPSv2's efficacy in forecasting real-time events with a four-week lead time. Incorporating ERPSv2 adds a practical dimension, enhancing HW predictions and facilitating timely responses to extreme heat events, crucial for public health measures and climate resilience planning in the face of escalating HW occurrences.

Keywords Heat wave · Spatial and temporal intensification · Large-scale features · SEDI scores · Subseasonal prediction

1 Introduction

One of the dangerous extreme temperature phenomena is heat wave (HW). Extreme heat can severely impact human health, disrupt energy and transportation systems, reduce agricultural productivity, strain water resources, and cause significant loss of life, particularly among vulnerable populations (Lee et al. 2019). According to earlier research (Black et al. 2004; Meehl and Tebaldi 2004; Perkins 2015), HWs are typically linked to anticyclonic circulations in the middle and upper troposphere, which extend into the lower troposphere and dynamically cause strong subsidence, clear skies, warm air advection, and leading to hot conditions at the surface. There are other factors that modulate the HWs. For example, extremely high night-time temperatures and high humidity levels persisted for at least three days during the Chicago HW, resulting in severe heat exhaustion (Karl and Knight 1997). During the record-breaking summer temperatures in 2003 over central Europe, there were highly extreme mean temperature conditions that lasted for longer than two weeks, though the humidity was not very high (Schär et al. 2004; Fischer and Schär 2010). The development of a persistent anticyclonic circulation in the upper

✉ Raju Mandal
raju.cat@tropmet.res.in

[1] Indian Institute of Tropical Meteorology, Pune 411008, India

level of the atmosphere results in the formation of a high-pressure system, which is responsible for long-lasting elevated temperature conditions over central Europe (Dole et al. 2011; Hudson et al. 2011; Matsueda 2011). The blocking highs in the upper atmosphere are found to be responsible for the generation of summer HWs in the USA and Europe (Teng et al. 2013; Pfahl et al. 2015). According to Parker et al. (2014), the HW over south-eastern parts of Australia is possibly linked with the upper-level anticyclonic potential vorticity anomalies that arise because of Rossby wave breaking. Three crucial synoptic scale elements were identified as the causes of the Russian HW in 2010 (Barriopedro et al. 2011): (1) an anomalous quasi-stationary anticyclonic circulation over western Russia; (2) a deficiency in accumulated precipitation from January to July; and (3) the loss of the early spring snow cover in western-central Russia. While anomalous atmospheric circulations are the source of many extreme temperature episodes, their propensity can be influenced by the basic sea surface temperature (SST) patterns (Arblaster and Alexander 2012; Trenberth and Fasullo 2012). In addition to the link between high temperatures and broad-scale atmospheric circulations, the role of the land surface and soil moisture in the emergence of HW has also been investigated (Seneviratne et al. 2006). Studies have speculated that land use change may play a significant role in modulating temperature extremes (Christidis et al. 2013; Wen et al. 2013). The Atlantic Multidecadal Oscillation is also known to influence the variation of HW frequency and duration (Sanderson et al. 2017).

The HWs in India happen from March to June (MAMJ), primarily over the north, northwest, central, and eastern coastal regions (Pai et al. 2013). It is well known that HWs over India are connected to climate modes like the El Niño-Southern Oscillation (ENSO) (De and Mukhopadhyay 1998). There has been a substantial increase in the HW day's frequency, persistency, and spatial coverage in recent years and they are also observed to be above average in the years following El Niño (Pai et al. 2013). The anomalous subtropical persistent high with the anticyclonic flow, the depletion of soil moisture over Indian land, and the anomalous SST anomalies across the tropical Indian and central Pacific Oceans are all connected to HWs over India (Rohini et al. 2016). Ratnam et al. (2016) identified two types of HW: (1) those that occur over north-central India and are linked to anomalous blocking over the North Atlantic Ocean, and (2) those that occur over coastal eastern India and are linked to an anomalous baroclinic Matsuno-Gill response to anomalous cooling in the Pacific. The examination of daily maximum and minimum temperature data from 121 stations across India from 1970 to 2005 revealed an overall increasing trend in the frequency of hot days and nights (Kothawale et al. 2010). According to recent studies, HWs will occur more frequently in India, where the populace is particularly vulnerable to extremely high temperatures (Im et al. 2017; Mazdiyasni et al. 2017). In significant sections of India's western and southern regions, the frequency of concurrent daytime and night-time HWs has increased since 1984 (Mukherjee and Mishra 2018). Researchers have demonstrated that the frequency of severe HWs will increase by 30 times under the increase in global mean temperature by the end of the twenty-first century (Mishra et al. 2017). Therefore, objective criteria must be implemented for the real-time monitoring and forecasting of such silently catastrophic events across the Indian region, considering the effects of such events on a range of societal sectors, including agriculture, health, and others. Besides the understanding of physical mechanisms and future projections of the HW, few studies (Russo et al. 2015; Lee et al. 2016; Pattanaik et al. 2017; Singh et al. 2017; Mandal et al. 2019) have attempted the prediction of these events using the anomalous temperatures and heat wave index (HWI) and particularly in Subseasonal scale.

This study analyses HW patterns in India and their association with large-scale atmospheric and ocean parameters. It uses a criterion based on the daily gridded maximum temperature (Tmax) data for the real-time prediction of HW over India on a subseasonal time scale during the summer season, MAMJ (following Mandal et al. 2019). This criterion has been implemented experimentally in the second version of the Extended Range Prediction System (ERPS), indigenously developed at the Indian Institute of Tropical Meteorology (IITM), Pune, India. A skilful forecast can disseminate useful, understandable, and timely information about such deadly events and can help reduce the adverse effects to a greater extent. Details of the datasets used, different methodologies and detailed results will be discussed in the following sections.

2 Data and methodology

2.1 Observation and reanalysis data

For the HW analysis, high-resolution daily gridded ($0.5° \times 0.5°$) observed Tmax datasets (1951–2023) have been obtained from the India Meteorological Department (IMD) (Srivastava et al. 2009). These datasets are available only on Indian land. The daily gridded ($2.5° \times 2.5°$) NCEP Reanalysis datasets (Kalnay et al. 1996) for geopotential height, u and v components of wind, and vertical velocity (omega) have been used for the composite analysis. The NOAA High-Resolution SST dataset (Reynolds et al. 2007; Huang et al. 2021) has been obtained to compute the composite anomalies of SST. For the composites, the reanalysis and SST datasets have been used from 1981 to 2020.

2.2 Model data

2.2.1 ERPSv2

The high resolution (0.5° × 0.5°) model datasets for Tmax, have been obtained from the second version of ERPS, which is built in-house at IITM, Pune, under the framework of Multi-Physics-Multi-Ensemble (MPME) (Sahai et al. 2021; Kaur et al. 2022). This prediction system is hereafter called the ERPSv2. The model simulations are conducted using the Climate Forecast System (CFS) model version 2 (CFSv2) of NCEP (Saha et al. 2014) with six different physics options. The idea of inter-model diversity has been integrated into the development of the ERPSv2 to address the errors arising from model physics. An alternative approach to explain these model errors has been proposed using a multi-physics ensemble scheme (Richardson 1997; Harrison et al. 1999; Orrell et al. 2001). In comparison to predictions based on a single physics model, the incorporation of multiple physical parameterisations has significantly outperformed the predictions through intra-model diversification (Berner et al. 2011; Tapiador et al. 2012; Greybush et al. 2017; Xu et al. 2020). The six physics options have been generated by combining two microphysics and three convective parameterisation schemes (Sahai et al. 2021; Kaur et al. 2022; Karmakar et al. 2023). The convection schemes include the Simplified Arakawa-Schubert (SAS) (Pan and Wu 1995), revised SAS (NSAS) (Han and Pan 2011) and NSAS with modified shallow-convection (NSAS_SC) (Han and Pan 2011). The microphysics schemes employed are Zhao and Carr (ZC) (Zhao and Carr 1997) and Ferrier (FER) (Ferrier et al. 2002). Note that runs from six different physics combinations are equivalent in all other respects. These combinations are then utilised to create the multi-physics ensemble (Sahai et al. 2021).

The models are initialised using the atmospheric initial conditions (ICs) (control and perturbed) from National Centre for Medium Range Weather Forecasting (NCMRWF) and the oceanic ICs from Indian National Centre for Ocean Information Services (INCOIS). The ERPSv2 has been implemented to generate the real-time forecast on an experimental basis from May 04, 2022. Initialisation of the model is continued at 7-day intervals until the end of April 2023. After this, the initialisation dates are kept the same as the previous year. The integrations are conducted in the seamless mode for thirty-six days; the first fifteen days include T574 resolution, while the remaining days involve T382. On the other hand, the ocean resolution stays unchanged during the integration duration. Model simulations are performed for six physics and with three ensembles (control + 2 perturbations) for each. Thus, a total of 18 members are made. The hindcast runs are made from 2003 to 2018 on the fly and the forecast is available for 2023 for the summer season MAMJ. The forecast/hindcast datasets have been used in the entire study after removing the climatological bias, which is discussed in detail in the next section.

2.2.2 ERPSv1

To calculate the skill scores and to compare the skill of ERPSv2 with the earlier version of ERPS, the hindcast datasets from 2003 to 2018 have been utilised from ERPSv1 (Abhilash et al. 2014b, 2015). These datasets are available on 1° × 1° horizontal resolution. The ERPSv1 includes two variants of CFSv2 and two variants of GFSv2 (run with the bias-corrected SST from CFSv2; (Abhilash et al. 2014a)) with spectral resolutions T126 (about 100 km) and T382 (about 38 km). Each of them has four ensembles. Thus, a total of 16 members are available. These datasets have been used after the bias correction following the same methodology.

2.3 Methodology

2.3.1 Heat wave criteria

While the IMD defines HWs using station-based Tmax data, its criteria are tailored to specific regions and stations. In contrast, the current study uses a gridded dataset with a 0.5° × 0.5° resolution, representing larger areas compared to individual stations, which typically cover approximately 25–50 km. This provides a more comprehensive view of regional HW patterns. The criteria used in this study, as formulated by Mandal et al. (2019) using Tmax, are designed for gridded data and can be applied to both model and observational datasets. It includes thresholds based on actual temperature values (using regional climatology), deviations from normal (comparable to IMD's approach), and percentile values, ensuring a consistent method across the subcontinent while accounting for regional variations. The following are the criteria: a HW day is considered if:

i. Its Tmax is > 36 °C and ≥ the climatological 95th percentile value (derived from daily temperatures during MAMJ) and also its deviation from the mean is > 3.5 °C on that day. Or,
ii. Its Tmax is > 44 °C.

The daily climatology is calculated during the period 1981–2010. The climatological 95th percentile of Tmax is calculated from daily values during MAMJ and for 1981–2010.

2.3.2 Identification of HW spells

The HW spells over two HW-prone regions, namely northwest (NW) and south-east (SE), have been identified following the criteria from (Mandal et al. 2019). These spells are determined based on the area-averaged daily Tmax values exceeding a threshold of 43°C and 40°C for a minimum of 6 consecutive days for NW and SE, respectively. Notably, it is observed that few spells exhibited overlapping periods, moving from NW to SE region. Then, to gain deeper insights, these spells with at least one overlapping day are segregated as NWSE spells. Subsequently, large-scale meteorological parameters associated with these three types of HW spells (hereafter NW-spell, SE-spell and NWSE-spell) have been examined. During the period 1981–2020, twenty-two events (total 212 HW days) as NW-spell, sixteen (total 154 HW days) as SE-spell, and ten (total 201 HW days) as NWSE-spell have been found. Here, it is worth mentioning that the third type of spell is only considered for the composite analysis of large-scale parameters.

2.3.3 Bias correction technique

In this study, the bias correction has been performed by removing the daily mean bias (model climatology–observed climatology) for the corresponding lead time. The bias correction method can be expressed as,

$$F_{bc}(t) = F_{raw}(t) - F_{c\,\mathrm{lim}}(t) + O_{c\,\mathrm{lim}}(t) \quad (1)$$

where, $F_{bc}(t)$, $F_{raw}(t)$, $F_{clim}(t)$, $O_{clim}(t)$ and t represent the bias-corrected forecast, raw forecast, model climatology, observed climatology and forecast lead time, respectively. The daily model and observed climatology have been calculated over the hindcast period from 2003 to 2018.

2.3.4 Statistical skill score

The Symmetric extremal dependence index (SEDI) (Ferro and Stephenson 2011) has been utilised to analyse the skill of the ERPSv2 in predicting the HWs during MAMJ. The key benefit of this index, which is ideal for extremely rare binary events, is that it is base-rate independent, which lowers stability and confidence (North et al. 2013). It accounts for the number of hits, false alarms, misses, and correct rejections. SEDI handles the model's "successful" and "unsuccessful" predictions. So, to utilise this index for probabilistic forecast verification, a threshold needs to be specified (Haiden et al. 2014; Mandal et al. 2023). So, in this study, fixing the probability as the threshold, the four elements of the contingency table are calculated. This index is defined as follows:

$$SEDI = \frac{\log F - \log H - \log(1-F) + \log(1-H)}{\log F + \log H + \log(1-F) + \log(1-H)}, (-1 \le SEDI \le 1) \quad (2)$$

where H is the hit rate and F is the false alarm rate. The perfect score is 1, and a positive score indicates better skill of the model than the random forecast.

The SEDI scores for different thresholds probabilities have been evaluated during the hindcast period 2003–2018 from ERPSv2 and ERPSv1.

3 Results and discussions

3.1 Spatio-temporal variability of HWs in India

3.1.1 Decadal variation of HWs

Applying the HW criterion developed by Mandal et al. (2019), the average number of HW days per decade for the summer season (MAMJ) and individual months, namely March, April, May, and June, spanning the period from 1951 to 2020, was computed. Subsequently, HW-days anomalies for each decade were obtained by comparing the calculated values against the climatological HW-days for the entire reference period (1951–2020). This comprehensive analysis provides insights into the evolving patterns of HW occurrences, highlighting deviations from the climatological norms and facilitating a detailed understanding of the temporal and spatial dynamics of HWs in the region. Figure 1 visually represents the decade-wise spatial distribution of HW-day anomalies observed during MAMJ for all seven decades (mentioned over each subplot). Remarkably, a significant change is observed, particularly in the recent three decades (Fig. 1e–g). The positive anomalies (more than 3 HW-days/decade) in HW-days are observed over the northwest, central and southeastern regions. This is more significant in the most recent decade, i.e., 2011–2020. This indicates a substantial increase in the occurrence of HW days, predominantly concentrated over the northwest, central, and southeastern regions of the country. Notably, this temporal pattern is accompanied by a noticeable spatial expansion towards southern India in recent decades.

Similarly, the month-wise analysis of the number of decade-average HW-days anomalies sheds light on subtle patterns across different regions of India (please refer to the supplementary Figures S1–S4). It is noteworthy that the unusual HW events happen outside of the peak summer months. For example, March has exhibited a noticeable rise in HW days across several southern locations in recent times. Moving into April, the anomaly becomes widespread,

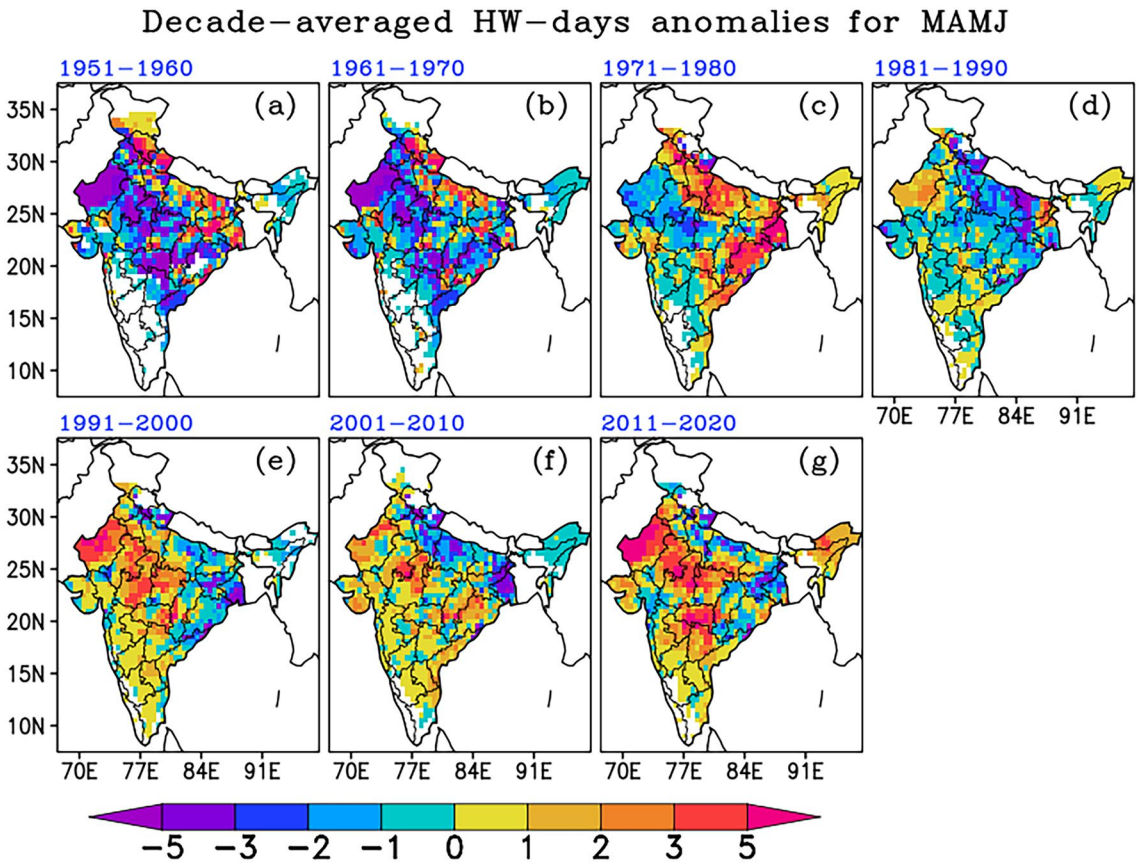

Fig. 1 Number of decade-averaged heat wave (HW) day anomalies for different decades from March to June (MAMJ), spanning the years 1951–2020. The climatology is based on data from the entire period of 1951–2020

encompassing central, southern, and eastern parts of the country. May witnesses a shift, with heightened HW activity predominantly in the northwest, central, and select southern areas, notably excluding the eastern regions during recent decades. By June, the results reveal a significant HW occurrence in the northwest and southeastern coastal regions, highlighting the change in the spatial pattern of HW occurrences in recent decades.

Hence, it could be summarised that in the backdrop of global warming, the HW events tend to occur more over the northwest, central and significantly over southeastern coastal parts in recent times. It also indicates the spatial and temporal extension of extreme summer. This finding is extremely important as it highlights how vulnerable these areas are to unusually high temperatures, which might be damaging to ecosystems and human health.

3.1.2 Spatial trends in HWs

Furthermore, this study examines the spatial distribution of decadal trends in HW days from 1951 to 2020 during the MAMJ period and it is presented in Fig. 2. The color shades represent trend values, with black dots indicating

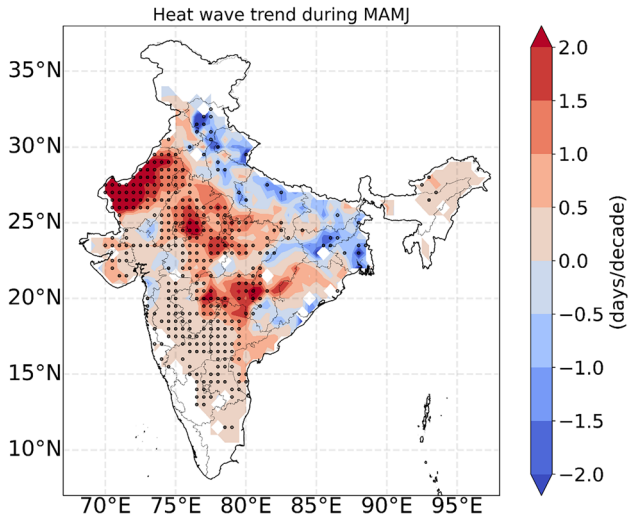

Fig. 2 Spatial distribution of decadal trends in HW days (days per decade) during the period MAMJ. The Mann–Kendall test was applied to assess trends at each grid point. Statistically significant trends ($p < 0.05$) are highlighted with black dots

statistically significant trends ($p < 0.05$) as determined by the Mann–Kendall test (Mann 1945; Kendall 1975). This analysis uses $0.5 \times 0.5°$ gridded Tmax data, providing a finer representation. The results show a notable increase in HW days per decade across northwest, central, southern, and southeastern India. Specifically, northwest and select central Indian regions experience an increase of 2 days or more per decade, whereas south and southeast India see an increase of 0.5 to 1 day per decade, though this rise is less pronounced than in northwest India. Statistically significant trends are observed across most parts of northwest, central, and southern India, with the exception of the extreme southern and southwestern regions. Conversely, certain areas in north and northeast India exhibit statistically significant decreasing trends, marked by negative values in blue. These results highlight the regional variability and intensity of HW trends.

3.1.3 Trends in the frequency and duration of HWs

The HW spells during MAMJ from 1951 to 2023 are considered for the analysis of temporal trends in HWs over the NW and SE HW-prone regions. Figure 3a represents the total number of HW days (colour bars) during MAMJ for each year from 1951 to 2023 for NW. The 11-year running mean (black-coloured solid line) is plotted along with this. The trend line is also shown with the red-coloured dashed line, and the corresponding p-value (calculated using the Mann–Kendall test and with a significance level of 0.05) is written on the right-top corner of the subplot. It is observed that there is a significant trend (p-value < 0.05) in the total number of HW days per year over the NW region. The increasing values of the 11-year running mean also indicate the rising trends in recent decades over this area.

The same analysis for the SE region is shown in Fig. 3b, where a more significant trend is observed (with a lower p-value than that of the NW region), indicating a stronger increasing trend in the total number of HW days per year. The p-value < 0.05 for the SE region shows a more significant trend in comparison to the NW region. The rising trend in the 11-year running mean in Fig. 3b further suggests a long-term change or shift in the total HW days per year over SE. Overall, the analysis demonstrates a general increase in the yearly total number of HW days in both regions, with SE showing a stronger trend, highlighting the increased persistence of HWs in recent decades.

In addition, this study examines the total HW days during MAMJ for each year, categorising events based on their duration (longer than seven days vs. seven days or less). Figure 4 illustrates the total number of HW days per year (with bars) during MAMJ, highlighting the linear trends (red dotted lines) and 11-year running means (black solid lines) for both long (> 7 days) and short (≤ 7 days) HW events in the NW and SE regions, with statistical significance assessed using the Mann–Kendall test. A significant trend (p-value < 0.05) in total HW days attributed to longer-duration events is observed for NW and SE regions (Fig. 4a, b). In comparison, neither region exhibits significant trends for shorter-duration events (Fig. 4c, d). This indicates that

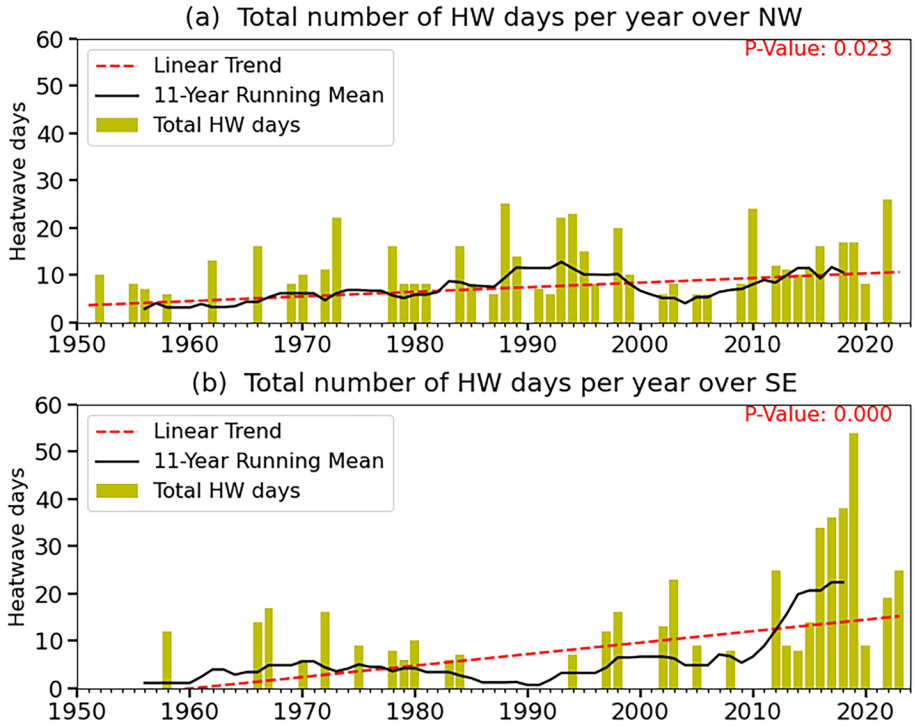

Fig. 3 Total number of HW days during MAMJ for each year (bars) for the **a** North-West (NW) region and **b** South-East (SE) region. The red dotted line and the black-coloured solid line represent the linear trend of HW days and the 11-year running mean, respectively, in each subplot. The p-values are calculated using the Mann–Kendall test

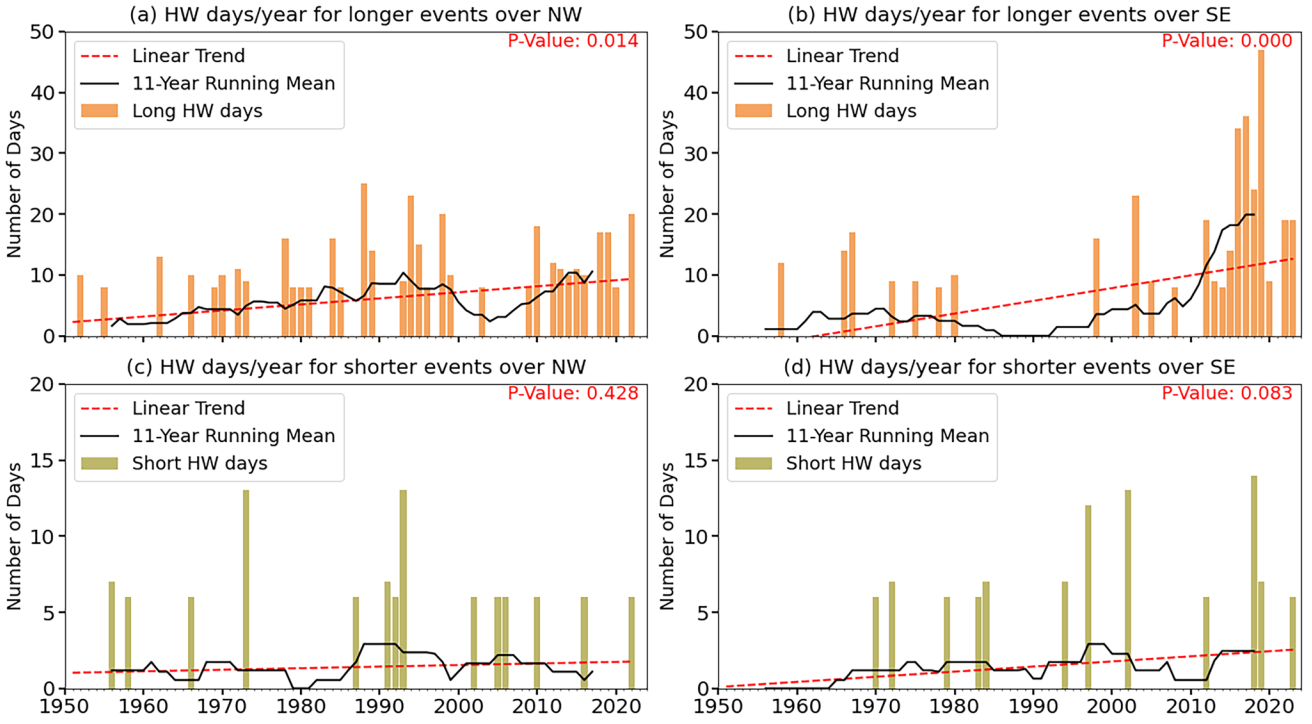

Fig. 4 Total number of HW days during MAMJ for each year (bars). The red dotted line and the black-coloured solid line represent the linear trend of HW days and the 11-year running mean, respectively, in each subplot. **a** for long (>7 days) HW events over the North-West (NW) region, **b** for long HW events over the South-East (SE) region, **c** for short (≤7 days) HW events over the NW region, and **d** for short (≤7 days) HW events over the SE region. [p-values are calculated using the Mann–Kendall test]

long-duration HW episodes have become more prevalent in recent years over both regions, which may have more significant adverse impacts on ecosystems, agriculture, and public health. At the same time, our analysis of seasonal mean and peak values of Tmax reveals no significant trends for either region, except notable trend in peak values over the NW region (please refer to the supplementary Figure S5). It highlights the complex nature of climate dynamics by integrating HW analysis with temperature trends. Notably, a comprehensive methodology is required for accurate climate change assessments and well-informed policy planning in these locations due to the association between variations in temperature and the documented trends in longer-duration HW events.

3.2 Large-scale features associated with HWs in India

A comprehensive composite analysis has been carried out to investigate the large-scale parameters associated with the three types of HW spells over India: NW, SE, and NWSE spells. The total number of spells and days included in the analysis for each category are as follows: NW spells (22 events, 212 days), SE spells (16 events, 154 days), and NWSE spells (11 events, 210 days), covering the duration from 1981 to 2020. The composite analysis involves examining anomalies in geopotential height at the 200 hPa level (gph200), vertical velocity at the 700 hPa level (omega700), wind vectors at the 925 hPa level (wind925) with colour-shaded magnitudes, and SST. Figures 5, 6, and 7 illustrate these composite anomalies for NW, SE, and NWSE spells, respectively.

The composite anomalies of gph200 during NW-spells indicate the presence of positive height anomalies over northern India (Fig. 5a). The unusually high pressure over northern India is not associated with the classical blocking patterns; instead, it is attributed to a subtropical high, which is commonly referred to as a persistent high (Perkins 2015). This stagnant high pressure creates a heated mass of air that stays stationary for several days, trapping additional heat and reducing convection currents in the process. The high pressure creates a barrier by forcing the air mass to descend to the ground's surface, preventing heat from rising (Li et al. 2015). This leads to heating being trapped at the surface, resulting in warming over northwestern India. The omega700 in Fig. 5b indicates sinking motion (with positive values) over the north-western regions of the country. Strong north-westerly winds are observed at the lower (925 hPa) level (Fig. 5c), which favours warm, dry air advection from the northwest arid regions to enter the boundary

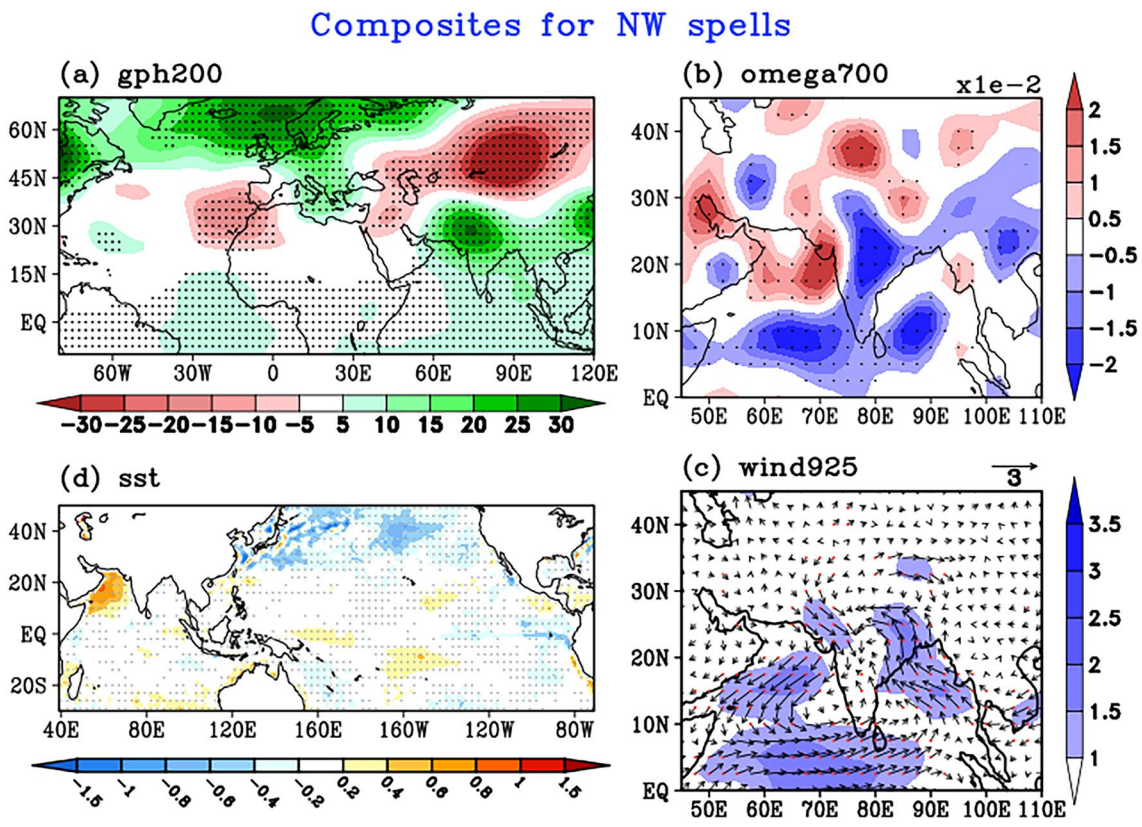

Fig. 5 Composite anomalies (clockwise) of **a** geopotential height (in m) at 200 hPa level, **b** Omega (in Pa/s) at 700 hPa level [positive/negative values represent sinking/rising motion], **c** wind vectors at 925 hPa level with magnitude (in m/s) in colour shade, and **d** sea surface temperature (in °C) for NW-spells. Black dots (purple dots in '**c**') denote the grids where the composite anomalies are statistically significant at 95% confidence level. This significance test has been performed using the Student's t-test

layer of NW parts of India. Additionally, significant positive SST anomalies are seen over the north-west Arabian Sea (Fig. 5d), which might have also influenced the HW over NW parts, as the high SSTs over the North Arabian Sea are positively correlated with the Tmax over the north-west HW zones of India (please refer to supplementary Figure S6). The Cross-correlation between SSTs and the north-west HW zone (23–30°N, 70–82°E) Tmax during MAMJ and for the period 1982–2021 has been computed and shown in Figure S6.

Figure 6 presents the composite anomalies of the same variables for SE-spells. It shows the existence of anomalous highs and lows over northern mid-latitudes and a quasi-stationary Rossby wave pattern (Fig. 6a). Positive gph200 anomalies are also observed across central, southeast, and northeast India at 200 hPa level, which causes strong subsidence (positive omega700 anomalies) over the central part of the country (Fig. 6b). This subsidence might cause a decrease in cloud cover, which could allow for greater shortwave radiation to reach the surface. Further, anomalous divergent winds at lower levels (wind925) are seen moving out of the southeast parts of India (Fig. 6c), resulting in an absence of strong sea breeze over south-eastern coastal areas (Singh and Kumar 2018), thereby accelerating HW-like conditions. Earlier researchers showed that the tropical Indian Ocean's warming as a result of global warming (Zheng et al. 2011) could increase the surface air temperature anomalies and aggravate HWs over the Indian subcontinent (Rohini et al. 2016; Qin et al. 2023). Additionally, it is found that the El Niño episodes have an impact on the HWs over the SE region by influencing the southwesterly wind patterns (Murari et al. 2016). Figure 6d shows high SST values over the Indian Ocean and the Pacific Niño region, indicating their association with the occurrence of HWs over the SE parts of India.

In the case of NWSE-spells, the composite anomalies are provided in Fig. 7. Over the North Atlantic and central Asia, respectively, the anomalous pattern of blocking high-pressure systems and upper tropospheric cyclones along with a quasi-stationary Rossby wave pattern over northern mid-latitudes, have been observed (Fig. 7a). An anomalous high is seen across the whole of India, with a large amplitude over the central and northern sides. Concurrently, the positive omega700 anomalies (sinking motion) are seen over

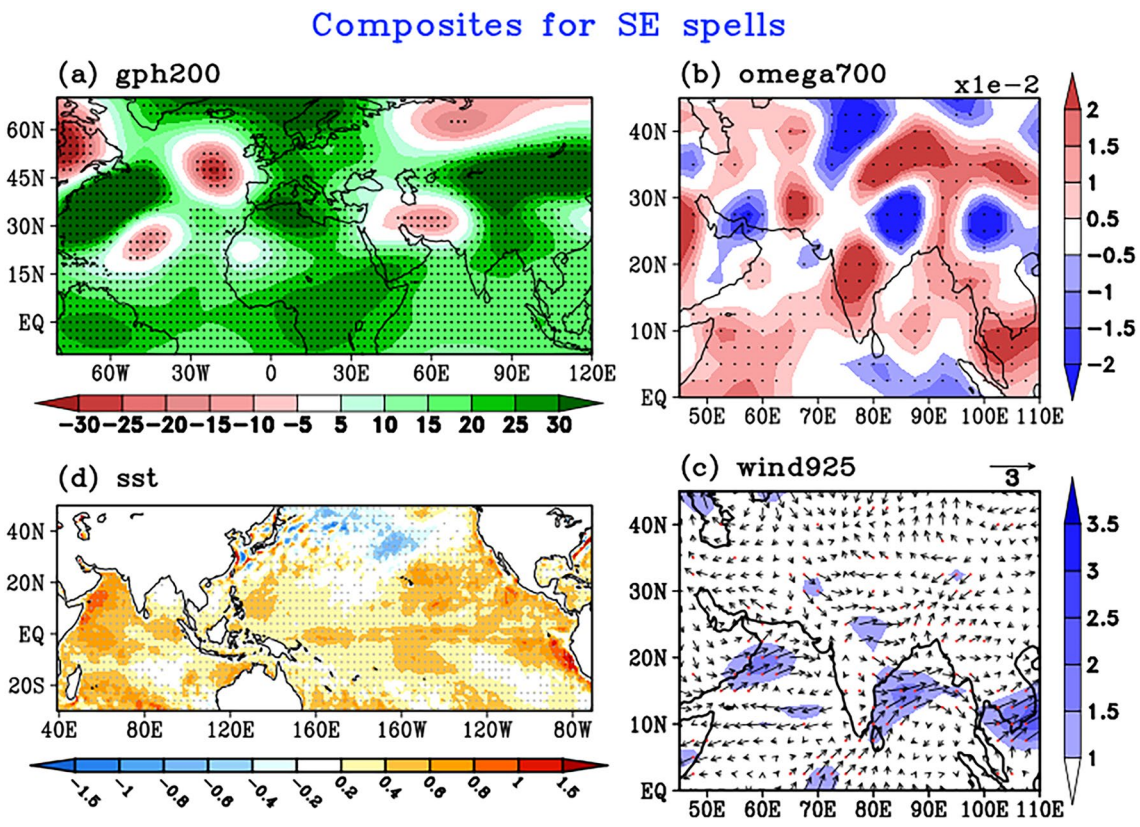

Fig. 6 Same as Fig. 5, but for SE-spells

the NW, central and SE regions (Fig. 7b). Low-level wind anomalies indicate that during such HW periods, northwesterly winds prevail over NW parts and move towards the SE regions (Fig. 7c). So, it can be speculated that typically HW originates over NW India and moves slowly eastward and southward, but not westward. While analysing the SST composites, significant positive anomalies prevail over the West Pacific and Equatorial Indian Ocean, with very high positive values over the Arabian Sea (Fig. 7d). The strong correlation between the higher SST values over these regions and the Tmax over the Indian subcontinent (Naveena et al. 2021) suggests their roles in influencing the HWs over NWSE regions.

Overall, the warming of the Indo-Pacific Oceans, and atmospheric forcing (subtropical highs, strong sinking motion and surface winds) are found to be significant factors associated with the occurrence of HWs in the Indian subcontinent.

3.3 Prediction skill on a subseasonal scale

Since the Tmax datasets have been used for the HW criterion, it is necessary to see the ERPS' skill in predicting the Tmax during the HW season first. Therefore, the anomaly correlation coefficient (ACC) (significant at 99.9% significance level) for Tmax during MAMJ has been computed for all subdivisions of India, considering a four-week (W1–W4) lead time. ACC values have been calculated by first preparing the area-averaged data for each subdivision utilising the 0.5° × 0.5° Tmax observed and model datasets. Then, we computed the weekly mean data corresponding to the ICs during MAMJ for different week leads (up to 4 weeks). The weekly climatology for each region was based on the 2003–2018 period, and the anomalies were computed by subtracting this climatology from the corresponding week leads for observation and for model. Comparisons have been made between ERPSv2 and its predecessor, ERPSv1 (Mandal et al. 2019), with the results presented in supplementary Figure S7. Analysing the ACC skill scores for leads W1–W4, it is evident that ERPSv2 demonstrates enhanced predictive skills across most subdivisions in the HW-prone regions, particularly up to W3 leads. However, a relatively lower skill level is observed over a few subdivisions in central India at the W4 lead time.

Figure 8 depicts the SEDI values for ERPSv2 and calculated using the HW-criterion for MAMJ during the hindcast period 2003 to 2018. To evaluate the SEDI values, we have considered our probabilistic HW forecasts as deterministic forecasts by fixing different threshold probability values (e.g., 30%, 50% and 70% presented in this case) for

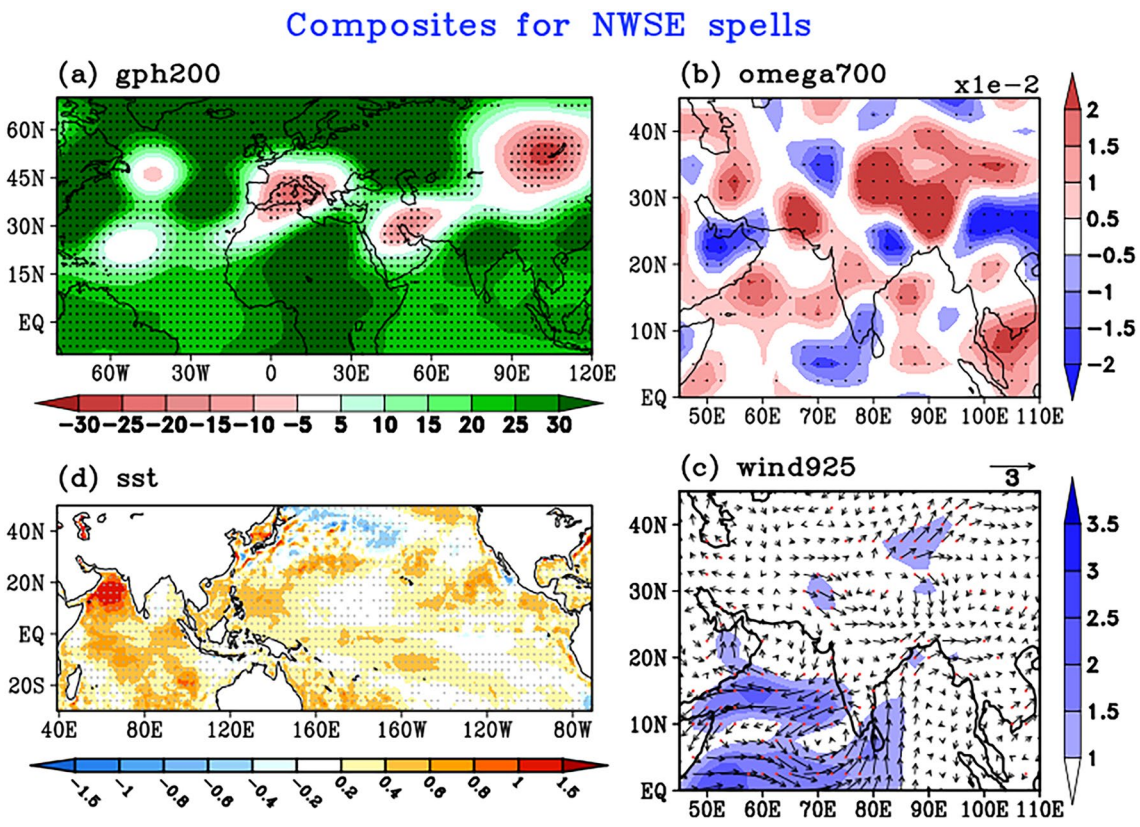

Fig. 7 Same as Fig. 5, but for NWSE-spells

the occurrence of HWs. This means it will consider the HW event as a binary event, whether the event is present with each of the probabilities as mentioned above in the ensemble forecasts. Figure 8a–l shows the week-wise (W1 to W4) SEDI values for 70% (Fig. 8a–d), 50% (Fig. 8e–h) and 30% (Fig. 8i–l) probabilities of HW occurrence. The positive SEDI values suggest that the forecast system is better than random, and higher positive values imply very good skill. Figures 8a, e, i show that the ERP system has exceptional skill in W1 lead in predicting the HW events (with 70% probability) over most parts of the HW-prone regions, particularly over northwest, central and south-eastern regions. In W2 lead (Fig. 8b, f, j) also it shows promising skills even with 70% probability over these regions, except very few parts in the south-eastern region for the higher probability threshold. With the 50% probability, even in W3 lead it gives skilful forecasts over northwest, central and a few parts of southeast coastal regions (Fig. 8g). But, with a 70% probability in W3 lead, it has good skills only over parts of northwest and central India. In the W4 lead, the ERPSv2 has excellent skills over most of the HW-prone regions but with low HW probability (e.g., here it is 30%) (Fig. 8l). It also shows reasonable skills over parts of central and southeast coastal regions with a 50% probability (Fig. 8h). Whereas, with higher probability, it exhibits very limited skills over only a few parts of the central India region (Fig. 8d).

Comparison of the SEDI scores of ERPSv2 with those of ERPSv1 (Mandal et al. 2019), as illustrated in Figure S8 in the Supplementary Information, demonstrates significantly improved skills of ERPSv2 up to W3 leads with 50% and 70% probability thresholds. ERPSv2 exhibits better skills in W4 lead over central and southeast coastal regions at a 50% probability threshold, and it also shows enhanced skills in W4 leads at lower probability thresholds such as 30%. Overall, the ERPSv2 shows improved and useful skills to predict the HW events with reasonable probabilities up to W3 lead time. However, with increasing lead and higher probability thresholds, the skill decreases.

3.4 Real-time performance of ERPSv2

This section assesses the model's ability (under the MPME framework) to capture the HW events in real-time mode. The HW criterion has been applied for real-time monitoring and prediction of HW in India on a subseasonal scale since March 2023 on an experimental basis using ERPSv2, which is a high-resolution forecasting system compared to ERPSv1. In Sect. 3.3, it is observed that ERPSv2 outperforms the earlier version, particularly in longer lead times.

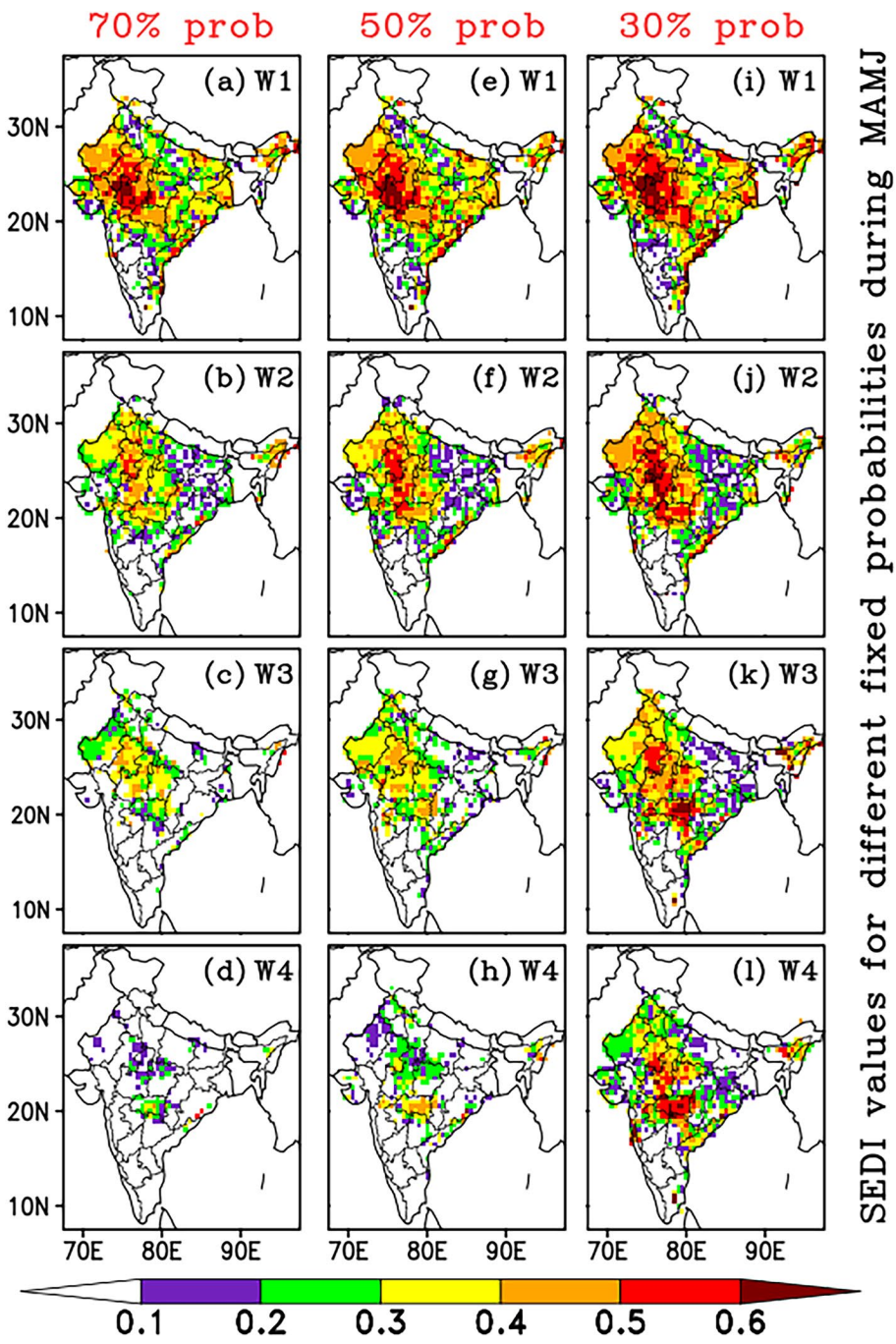

Fig. 8 The symmetric extremal dependence index (SEDI) scores for ERPSv2 during MAMJ for the hindcast period 2003–2018. **a–d** SEDI scores for 70% HW probability, **e–h** SEDI scores for 50% HW probability and **i–l** SEDI scores for 30% HW probability for different week leads. [ERPSv2 stands for the second version of the subseasonal prediction system of IITM, Pune]

Now, the efficiency of ERPSv2 in predicting HW spells over the Indian region is evaluated through the verification of a recent HW event. In the initial half of June 2023, eastern India experienced a severe HW while Cyclonic Storm "Biparjoy" persisted over the Arabian Sea from June 6–16, later making landfall in India from June 16–19. It was a notable episode of intense heat in the eastern portions of the country, with the average maximum temperature reaching the third-highest since 1901, behind 1979 and 1958, and the average lowest temperature reported as the second-highest since 1958 (please refer to the supplementary Figure S9). Using the HW spell identification criteria, this spell has been identified as SE-spell and during June 02–15, 2023. From the observed Tmax anomalies during 02–15 June, it is seen that the affected areas include West Bengal, Odisha, Bihar, east Uttar Pradesh, Jharkhand, Chhattisgarh, and Coastal Andhra Pradesh (Fig. 9a). Where Tmax anomalies are observed between 4 and 5 °C. The delayed monsoon onset (8th June, one week later than its normal onset date of June 1) over Kerala and the presence of strong El Niño

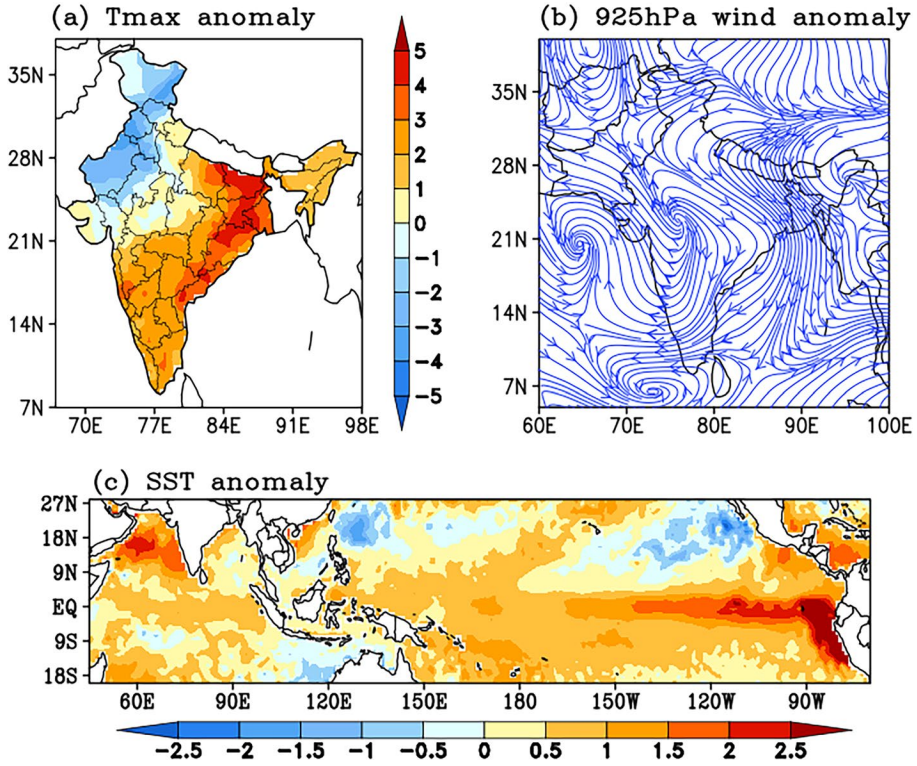

Fig. 9 **a** Tmax anomalies (℃), **b** wind anomalies (streamline) at 925 hPa level, and **c** SST anomalies (℃) for the HW event from 02 to 15 June 2023

condition over Eastern Pacific during the first half of June 2023 (Fig. 9c), might have impacted the Tmax over Indian region by influencing the circulation (e.g., southwesterly) patterns (Murari et al. 2016). The anomalies in lower-level winds (at 925 hPa) suggest strong winds coming from arid and hot north-western regions, blowing away from the Indian subcontinent (Fig. 9b), resulting in an absence of strong sea breeze over south-eastern coastal areas (Singh and Kumar 2018). This atmospheric condition likely contributed to the development of the HW situation in the eastern regions.

The efficiency of ERPSv2 in predicting this event is verified by computing the probability of its occurrence from observations and the model. Forecast verification is presented for two target weeks: (i) week1: June 2–8, 2023, and (ii) week2: June 9–15, 2023, in Fig. 10. The observed HW probabilities are shown in the leftmost panels (Fig. 10a, f), while the subsequent panels to the right (Fig. 10b–e, g–j) represent the model-predicted values for the four nearest ICs (written in the format IC: MMDD on the top of each subpanel) for the two target weeks. From the observation in Fig. 10a, it is evident that the observed HW probabilities are very high (moderate) over Bihar, Gangetic West Bengal and Assam and Arunachal Pradesh (coastal Odisha and Andhra Pradesh) subdivisions during the week1. In the week2, the spatial coverage of very high HW probability increases, mainly observed over east Uttar Pradesh, Bihar, Gangetic West Bengal, Jharkhand, Odisha, coastal Andhra Pradesh and parts of Chhattisgarh (Fig. 10f). The model effectively captures the occurrence of HW during week1 from 1st June and 25th May ICs with very high probability (Fig. 10b, c). From W3 and W4 leads (Fig. 10d, e), it also captures the event reasonably well with medium probability. Predictions for week2 show a well-forecasted severe HW condition from all four-week lead forecasts (Fig. 10g–j). However, the W4 lead forecast (Fig. 10j) displays medium HW probabilities over those subdivisions and slight over-predictions over some areas of central and northwest India. Overall, ERPSv2 proves to be beneficial for HW prediction in these regions with a four-week lead time, albeit with relatively less confidence at the W4 lead.

4 Summary and conclusions

This work presents a thorough analysis of HWs in India from 1951 to 2020, with an emphasis on the trends, decadal variability, and associated large-scale features. The average number of HW days for each decade and anomalies are calculated using a HW criterion developed by Mandal et al. (2019). The findings show a considerable rise (more than 3 HW-days/decade) in the occurrence of HWs over the central, southeast, and northwest regions during post-2000, indicating a temporal and spatial intensification of extreme summer conditions. The anomalously high HW days in recent decades carry substantial significance, warranting urgent attention and adaptive measures. The intensification

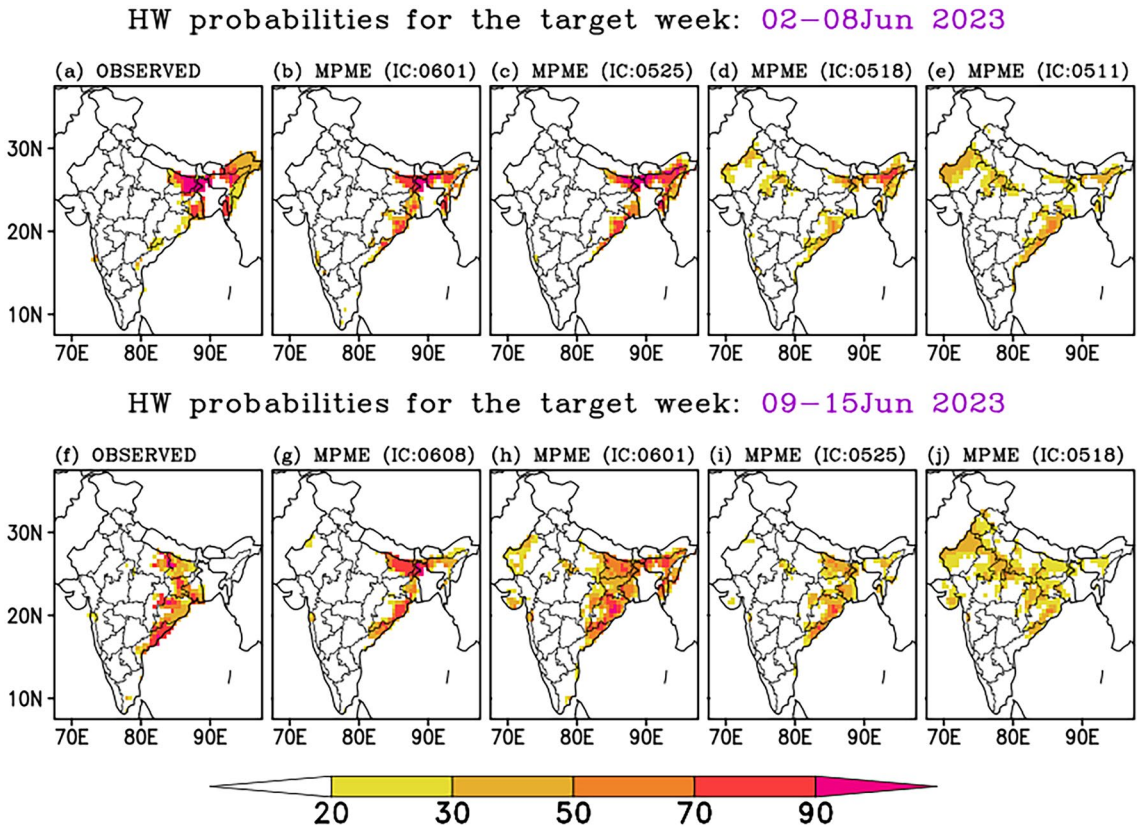

Fig. 10 The probabilities of occurrence of HWs for the target weeks: **a–e** 02–08 June 2023 and **f–j** 09–15 June 2023. The leftmost panels represent the observed, and the subsequent panels towards the right represent the model-predicted values for the four nearest initial conditions (written in the format IC: MMDD)

and spatial expansion of HW pose enormous challenges for agriculture, water resources, and public health, necessitating a proactive and region-specific approach to climate resilience and mitigation strategies. This study contributes valuable insights into the evolving climate patterns in India, serving as a crucial reference for policymakers, researchers, and practitioners engaged in climate change adaptation and mitigation efforts.

Monthly analyses of decadal average HW-day anomalies reveal subtle variations in patterns, with significant HW events occurring beyond the summer's hottest months. For example, March shows an increase in HW days (1 day/decade) over few parts of southern region compared to the previous decades. The dynamic character of HW events is highlighted, with notable impacts observed, such as an increase of 3 days/decade in June across central and northwest parts. This knowledge is essential for understanding how different regions are susceptible to high temperatures, which could endanger ecosystems and public health.

An analysis of spatial HW trends reveals a significant increase in total HW days/year over northwest, central, and southeast India. Conversely, certain areas in north and northeast India show decreasing trends, explicitly highlighting the location-specific dynamics of HW events. The study also analyses HW spells in the NW and SE regions from 1951 to 2023 during the MAMJ period. In both regions, there is a significant increasing trend in the total number of HW days per year, evident from both the 11-year running mean and trend line, suggesting a long-term change possibly linked to climate change. Additionally, the research notes a rise in longer-duration HW events over HW-prone regions in recent years, which holds potential implications for ecosystems, agriculture, and public health. Meanwhile seasonal mean and peak temperature values exhibit complex dynamics, emphasising the need for a comprehensive approach in climate change assessments and policy planning.

The study investigates large-scale characteristics linked to different kinds of HW spells, emphasising the significance of the oceans and atmospheric variables on HW patterns. The investigation of the functions of subtropical highs, sinking motion, wind patterns, and SSTs yields knowledge of the factors influencing the occurrence of HW on the Indian subcontinent.

Furthermore, ERPSv2 is introduced in the manuscript, and its subseasonal prediction skill is assessed. When compared to ERPSv1, it performs better and shows enhanced

predictive ability, especially up to three-week leads. This improvement can be attributed to the adoption of a multi-physics ensemble approach in ERPSv2, which, as demonstrated by Kaur et al. (2022), reduces model uncertainties and enhances forecast reliability by increasing ensemble dispersion. Additionally, the incorporation of multiple ensembles further refines the probabilistic forecasting. These advancements significantly improve the extended range prediction of HW events, particularly over regions vulnerable to HWs. The study offers insightful information about ERPSv2's ability to forecast, which has implications for understanding and predicting HW events in such vulnerable areas.

The effectiveness of ERPSv2 in forecasting real-time HW events is validated by a case study on a disastrous HW event that occurred in June 2023. The model shows its usefulness in forecasting HWs with a four-week lead time by effectively capturing the temporal and spatial characteristics of the observed occurrence.

In summary, this work contributes to our understanding of the dynamics of HW in India by emphasising the changing trends, patterns, and large-scale associated features. The work gains a practical aspect by incorporating ERPSv2 and its validation with real-time data, proving its potential to enhance HW predictions and facilitate timely responses to extreme heat occurrences. The findings delivered here have implications for public health measures and planning for climate resilience given the region's increasing occurrences of HWs.

Supplementary Information The online version contains supplementary material available at https://doi.org/10.1007/s00382-024-07539-x.

Acknowledgements IITM is fully supported by the Ministry of Earth Sciences, Govt. of India, New Delhi. We thank National Centre for Medium Range Weather Forecasting (NCMRWF) and Indian National Centre for Ocean Information Services (INCOIS) for providing the initial conditions to simulate the models. We acknowledge NCEP for technical support on the CFS model. We want to express our sincere gratitude to the India Meteorological Department (IMD) for preparing the high-resolution maximum temperature observation datasets over the Indian region and NOAA/OAR/ESRL PSL for making available the NCEP reanalysis. During the analysis, the technical support of the HPC (High-Performance Computing facility installed at IITM, named PRATYUSH) support team is highly appreciated.

Author contributions R.M. and S.J. conceptualised the study. Most of the analysis was performed by R.M., and S.J., A.C., and S.W. made significant contributions in some of the analysis. R.M. led the manuscript writing and the original manuscript was prepared by R.M. Contributions were made in performing the model runs by R.M., A.D., M.K. and S.W. All authors contributed to the editing of the manuscript and interpretations of the results.

Funding No separate funding has been utilised for this work.

Data availability The high-resolution IMD observation maximum temperature datasets are obtained from IMD Pune which is not available publicly. But the $1^\circ \times 1^\circ$ datasets are available at "https://www.imdpune.gov.in/lrfindex.php". The NCEP reanalysis has been downloaded from https://psl.noaa.gov/data/gridded/data.ncep.reanalysis.pressure.html. The subseasonal prediction model datasets of IITM, Pune may be available upon request to the corresponding author.

Code availability Analytical scripts and programming used in this study are available from the corresponding author upon reasonable request.

Declarations

Conflict of interest The authors declare no competing interests.

Ethical approval The manuscript has not been submitted to more than one journal for simultaneous consideration. The manuscript has not been published elsewhere previously.

Consent to participate Not Applicable.

Consent for publication Not Applicable.

References

Abhilash S, Sahai AK, Borah N et al (2014a) Does bias correction in the forecasted SST improve the extended range prediction skill of active-break spells of Indian summer monsoon rainfall? Atmos Sci Lett 15:114–119. https://doi.org/10.1002/asl2.477

Abhilash S, Sahai AK, Pattnaik S et al (2014b) Extended range prediction of active-break spells of Indian summer monsoon rainfall using an ensemble prediction system in NCEP Climate Forecast System. Int J Climatol 34:98–113. https://doi.org/10.1002/joc.3668

Abhilash S, Sahai AK, Borah N et al (2015) Improved spread-error relationship and probabilistic prediction from the CFS-based grand ensemble prediction system. J Appl Meteorol Climatol 54:1569–1578. https://doi.org/10.1175/JAMC-D-14-0200.1

Arblaster JM, Alexander LV (2012) The impact of the El Nio-Southern Oscillation on maximum temperature extremes. Geophys Res Lett 39:2–6. https://doi.org/10.1029/2012GL053409

Barriopedro D, Fischer EM, Luterbacher J et al (2011) The hot summer of 2010: map of Europe. Science 332:220–224

Berner J, Ha SY, Hacker JP et al (2011) Model uncertainty in a mesoscale ensemble prediction system: Stochastic versus multiphysics representations. Mon Weather Rev 139:1972–1995. https://doi.org/10.1175/2010MWR3595.1

Black E, Blackburn M, Harrison G et al (2004) Factors contributing to the summer 2003 European heatwave. Weather 59:217–223. https://doi.org/10.1256/wea.74.04

Christidis N, Stott PA, Scaife AA et al (2013) A new HADGEM3-a-based system for attribution of weather- and climate-related extreme events. J Clim 26:2756–2783. https://doi.org/10.1175/JCLI-D-12-00169.1

De US, Mukhopadhyay RK (1998) Severe heat wave over the Indian subcontinent in 1998, in perspective of global climate. Curr Sci 75:1308–1311

Dole R, Hoerling M, Perlwitz J et al (2011) Was there a basis for anticipating the 2010 Russian heat wave? Geophys Res Lett 38:1–5. https://doi.org/10.1029/2010GL046582

Ferrier BS, Jin Y, Lin Y et al (2002) Implementation of a new grid-scale cloud and precipitation scheme in the NCEP eta model. 15th conference on numerical weather prediction. American Meteorological Society, San Antonio, pp 280–283

Ferro CAT, Stephenson DB (2011) Extremal dependence indices: improved verification measures for deterministic forecasts of rare binary events. Weather Forecast 26:699–713. https://doi.org/10.1175/WAF-D-10-05030.1

Fischer EM, Schär C (2010) Consistent geographical patterns of changes in high-impact European heatwaves. Nat Geosci 3:398–403. https://doi.org/10.1038/ngeo866

Greybush SJ, Saslo S, Grumm R (2017) Assessing the ensemble predictability of precipitation forecasts for the January 2015 and 2016 East Coast winter storms. Weather Forecast 32:1057–1078. https://doi.org/10.1175/WAF-D-16-0153.1

Haiden T, Magnusson L, Richardson D (2014) Statistical evaluation of ECMWF extreme wind forecasts. ECMWF Newsletter No 139—Spring 2014

Han J, Pan HL (2011) Revision of convection and vertical diffusion schemes in the NCEP Global Forecast System. Weather Forecast 26:520–533. https://doi.org/10.1175/WAF-D-10-05038.1

Harrison MSJ, Palmer TN, Richardson DS, Buizza R (1999) Analysis and model dependencies in medium-range ensembles: two transplant case-studies. Q J R Meteorol Soc 125:2487–2515. https://doi.org/10.1002/qj.49712555908

Huang B, Liu C, Banzon V et al (2021) Improvements of the daily optimum interpolation sea surface temperature (DOISST) version 2.1. J Clim 34:2923–2939. https://doi.org/10.1175/JCLI-D-20-0166.1

Hudson D, Marshall AG, Alves O (2011) Intraseasonal forecasting of the 2009 summer and winter Australian heat waves using POAMA. Weather Forecast 26:257–279. https://doi.org/10.1175/WAF-D-10-05041.1

Im ES, Pal JS, Eltahir EAB (2017) Deadly heat waves projected in the densely populated agricultural regions of South Asia. Sci Adv 3:1–8. https://doi.org/10.1126/sciadv.1603322

Kalnay E, Kanamitsu M, Kistler R et al (1996) The NCEP/NCAR 40-year reanalysis project. Bull Am Meteorol Soc 77:437–471. https://doi.org/10.1175/1520-0477(1996)077%3c0437:TNYRP%3e2.0.CO;2

Karl TR, Knight RW (1997) The 1995 Chicago heat wave: how likely is a recurrence? Bull Am Meteorol Soc 78:1107–1119. https://doi.org/10.1175/1520-0477(1997)078%3c1107:TCHWHL%3e2.0.CO;2

Karmakar N, Joseph S, Sahai AK et al (2023) Northward propagation of convection over the Indian region in multiphysics multimodel ensemble. Q J R Meteorol Soc 149:231–246. https://doi.org/10.1002/qj.4404

Kaur M, Sahai AK, Phani R et al (2022) Multi-physics schema for sub-seasonal prediction of Indian summer monsoon. Clim Dyn 58:669–690. https://doi.org/10.1007/s00382-021-05926-2

Kendall MG (1975) Rank correlation methods. Oxford University Press, New York

Kothawale DR, Revadekar JV, Kumar KR (2010) Recent trends in pre-monsoon daily temperature extremes over India. J Earth Syst Sci 119:51–65. https://doi.org/10.1007/s12040-010-0008-7

Lee HJ, Lee WS, Yoo JH (2016) Assessment of medium-range ensemble forecasts of heat waves. Atmos Sci Lett 17:19–25. https://doi.org/10.1002/asl.593

Lee V, Zermoglio F, Ebi K (2019) Heat waves and human health—emerging evidence and experience to inform risk management in a warming world. United States Agency for International Development, Washington, pp 1–53

Li D, Sun T, Liu M, Yang L, Wang L, Gao Z (2015) Contrasting responses of urban and rural surface energy budgets to heat waves explain synergies between urban heat islands and heat waves. Environ Res Lett 10:054009. https://doi.org/10.1088/1748-9326/10/5/054009

Mandal R, Joseph S, Sahai AK et al (2019) Real time extended range prediction of heat waves over India. Sci Rep. https://doi.org/10.1038/s41598-019-45430-6

Mandal R, Joseph S, Sahai AK et al (2023) Diagnostics and real-time extended range prediction of cold waves over India. Clim Dyn 61:2051–2069. https://doi.org/10.1007/s00382-023-06666-1

Mann HB (1945) Nonparametric tests against trend. Econometrica 13:245–259

Matsueda M (2011) Predictability of Euro-Russian blocking in summer of 2010. Geophys Res Lett 38:1–6. https://doi.org/10.1029/2010GL046557

Mazdiyasni O, AghaKouchak A, Davis SJ et al (2017) Increasing probability of mortality during Indian heat waves. Sci Adv 3:1–6. https://doi.org/10.1126/sciadv.1700066

Meehl GA, Tebaldi C (2004) More intense, more frequent, and longer lasting heat waves in the 21st century. Science 305:994–997

Mishra V, Mukherjee S, Kumar R, Stone DA (2017) Heat wave exposure in India in current, 15 °c, and 20 °c worlds. Environ Res Lett. https://doi.org/10.1088/1748-9326/aa9388

Mukherjee S, Mishra V (2018) A sixfold rise in concurrent day and night-time heatwaves in India under 2 °C warming. Sci Rep 8:1–9. https://doi.org/10.1038/s41598-018-35348-w

Murari KK, Sahana AS, Daly E, Ghosh S (2016) The influence of the El Niño Southern Oscillation on heat waves in India. Meteorol Appl 23:705–713. https://doi.org/10.1002/met.1594

Naveena N, Satyanarayana GC, Rao KK et al (2021) Heat wave characteristics over India during ENSO events. J Earth Syst Sci. https://doi.org/10.1007/s12040-021-01674-3

North R, Trueman M, Mittermaier M, Rodwell MJ (2013) An assessment of the SEEPS and SEDI metrics for the verification of 6h forecast precipitation accumulations. Meteorol Appl 20:164–175. https://doi.org/10.1002/met.1405

Orrell D, Smith L, Barkmeijer J, Palmer TN (2001) Model error in weather forecasting. Nonlinear Process Geophys 8:357–371. https://doi.org/10.5194/npg-8-357-2001

Pai DS, Nair SA, Ramanathan AN (2013) Long term climatology and trends of heat waves over India during the recent 50 years (1961–2010). Mausam 64:585–604

Pan HL, Wu WS (1995) Implementing a mass flux convection parameterization package for the NMC medium-range forecast model. NMC Office Note 409. Washington

Parker TJ, Berry GJ, Reeder MJ, Nicholls N (2014) Modes of climate variability and heat waves in Victoria, southeastern Australia. Geophys Res Lett 41:6926–6934. https://doi.org/10.1002/2014GL061736

Pattanaik DR, Mohapatra M, Srivastava AK, Kumar A (2017) Heat wave over India during summer 2015: an assessment of real time extended range forecast. Meteorol Atmos Phys 129:375–393. https://doi.org/10.1007/s00703-016-0469-6

Perkins SE (2015) A review on the scientific understanding of heatwaves—their measurement, driving mechanisms, and changes at the global scale. Atmos Res 164–165:242–267. https://doi.org/10.1016/j.atmosres.2015.05.014

Pfahl S, Schwierz C, Croci-Maspoli M et al (2015) Importance of latent heat release in ascending air streams for atmospheric blocking. Nat Geosci 8:610–614. https://doi.org/10.1038/ngeo2487

Qin J, Liu H, Li B (2023) Unprecedented warming in Northwestern India during April of 2022: roles of local forcing and atmospheric Rossby wave. Geosci Lett. https://doi.org/10.1186/s40562-022-00257-4

Ratnam JV, Behera SK, Ratna SB et al (2016) Anatomy of Indian Heatwaves. Sci Rep 6:1–11. https://doi.org/10.1038/srep24395

Reynolds RW, Smith TM, Liu C et al (2007) Daily high-resolution-blended analyses for sea surface temperature. J Clim 20:5473–5496. https://doi.org/10.1175/2007JCLI1824.1

Richardson D (1997) The relative effects of model and analysis differences on ECMWF and UKMO operational forecasts. In: Workshop on predictability, 20–22 October 1997. Shinfield Park, Reading

Rohini P, Rajeevan M, Srivastava AK (2016) On the variability and increasing trends of heat waves over India. Sci Rep 6:1–9. https://doi.org/10.1038/srep26153

Russo S, Sillmann J, Fischer EM (2015) Top ten European heatwaves since 1950 and their occurrence in the coming decades. Environ Res Lett. https://doi.org/10.1088/1748-9326/10/12/124003

Saha S, Moorthi S, Wu X et al (2014) The NCEP climate forecast system version 2. J Clim 27:2185–2208. https://doi.org/10.1175/JCLI-D-12-00823.1

Sahai AK, Kaur M, Joseph S et al (2021) Multi-model multi-physics ensemble: a futuristic way to extended range prediction system. Front Clim. https://doi.org/10.3389/fclim.2021.655919

Sanderson M, Economou T, Salmon K, Jones S (2017) Historical trends and variability in heat waves in the United Kingdom. Atmosphere (Basel) 8:191. https://doi.org/10.3390/atmos8100191

Schär C, Vidale PL, Lüthi D et al (2004) The role of increasing temperature variability in European summer heatwaves. Nature 427:332–336. https://doi.org/10.1038/nature02300

Seneviratne SI, Lüthi D, Litschi M, Schär C (2006) Land-atmosphere coupling and climate change in Europe. Nature 443:205–209. https://doi.org/10.1038/nature05095

Singh C, Kumar SVJ (2018) Meteorological conditions for development of heat wave over Coastal Andhra Pradesh and Telangana. J Ind Geophys Union 22:349–359

Singh H, Arora K, Ashrit R, Rajagopal EN (2017) Verification of pre-monsoon temperature forecasts over India during 2016 with a focus on heatwave prediction. Nat Hazards Earth Syst Sci 17:1469–1485. https://doi.org/10.5194/nhess-17-1469-2017

Srivastava AK, Rajeevan M, Kshirsagar SR (2009) Development of a high resolution daily gridded temperature data set (1969–2005) for the Indian region. Atmos Sci Lett 10:249–254. https://doi.org/10.1002/asl.232

Tapiador FJ, Tao WK, Shi JJ et al (2012) A comparison of perturbed initial conditions and multiphysics ensembles in a severe weather episode in Spain. J Appl Meteorol Climatol 51:489–504. https://doi.org/10.1175/JAMC-D-11-041.1

Teng H, Branstator G, Wang H et al (2013) Probability of US heat waves affected by a subseasonal planetary wave pattern. Nat Geosci 6:1056–1061. https://doi.org/10.1038/ngeo1988

Trenberth KE, Fasullo JT (2012) Climate extremes and climate change: the Russian heat wave and other climate extremes of 2010. J Geophys Res Atmos 117:1–12. https://doi.org/10.1029/2012JD018020

Wen QH, Zhang X, Xu Y, Wang B (2013) Detecting human influence on extreme temperatures in China. Geophys Res Lett 40:1171–1176. https://doi.org/10.1002/grl.50285

Xu Z, Chen J, Zheng J et al (2020) Assessment of the forecast skill of multiphysics and multistochastic methods within the GRAPES regional ensemble prediction system in the East Asian Monsoon Region. Weather Forecast 35:1145–1171. https://doi.org/10.1175/WAF-D-19-0021.1

Zhao Q, Carr FH (1997) A prognostic cloud scheme for operational NWP models. Mon Weather Rev 125:1931–1953

Zheng XT, Xie SP, Liu Q (2011) Response of the Indian Ocean basin mode and its capacitor effect to global warming. J Clim 24:6146–6164. https://doi.org/10.1175/2011JCLI4169.1